analytical chemistry

pubs.acs.org/ac Article

Versatile Luminol/Dissolved Oxygen/Fe@Fe_2O_3 Nanowire Ternary Electrochemiluminescence System Combined with Highly Efficient Strand Displacement Amplification for Ultrasensitive microRNA Detection

Jia-Li Liu,[†] Rong Yang,[†] Ya-Qin Chai,* and Ruo Yuan*

Cite This: *Anal. Chem.* 2021, 93, 13334−13341 Read Online

ACCESS | Metrics & More | Article Recommendations | Supporting Information

ABSTRACT: Herein, a versatile ECL biosensor was fabricated for ultrasensitive detection of microRNA-21 (miRNA-21) from cancer cells based on a novel H_2O_2-free electrochemiluminescence (ECL) system (luminol/dissolved oxygen/Fe@Fe_2O_3 nanowires). Compared with the previously reported coreaction accelerator that needed a negative potential to produce reactive oxygen species (ROS), these newly discovered Fe@Fe_2O_3 nanowires could generate ROS in the detection solution immediately without the application of voltage, which narrowed down the detection potential range to avoid side reactions, favoring their practical application in biological systems. Especially, the Fe@Fe_2O_3 nanowires could produce $H^{\bullet}$ for activating dissolved oxygen into ROS to improve the ECL intensity dramatically, which initiates a novel pathway to promote the generation of ROS for the ECL system. In addition, an original strand displacement amplification coupled with strand displacement reaction (SDA-SDR) was developed to improve the conversion efficiency of the target for sensitive detection of miRNA-21. By virtue of the SDR, a quadruple quenching effect was achieved through each output DNA strand of SDA; hence, the nucleic acid signal amplification efficiency was effectively enhanced. As expected, on account of the superb activation performance of Fe@Fe_2O_3 nanowires and the outstanding amplification efficiency of the SDR-SDA strategy, the fabricated ECL biosensor realized ultrasensitive detection of miRNA-21 with a detection limit down to 52.5 aM. The established ECL sensing platform ushered a new route for H_2O_2-free detection and a promising biomarker assay method for clinical diagnosis.

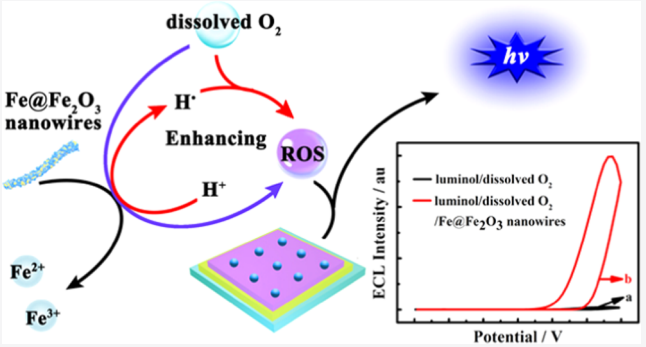

INTRODUCTION

MicroRNA (miRNA), a type of 20−25 nucleotides, noncoding, endogenous single-stranded RNA, has been reported to be closely related to emergence, deterioration, and transference processes of various kinds of cancers, *e.g.*, breast cancer, lung cancer, and prostatic carcinoma.[1,2] Therefore, highly sensitive detection of microRNA is helpful for early diagnosis and removal of malignant tumors to save and prolong patients' lives.[3] Currently, electrochemiluminescence (ECL) technology has arisen as a powerful analytical tool in clinical diagnosis for the detection of various cancer biomarkers, such as miRNA, protein, and exosome.[4−6] As a classical luminophore, luminol has received widespread attention over a long period due to its low excitation potential, high quantum yield, and nontoxicity.[7] However, H_2O_2 as a coreactant of luminol exhibits the defects of bio-toxicity and instability, which creates great difficulties for its application in bioassay. Therefore, an alternative resolution was to seek for a safe and efficient coreactant to replace H_2O_2. As an endogenous component existing in most biological systems, dissolved oxygen has been found to be a potential substitute for H_2O_2 as a coreactant.[8] Nonetheless, the low decomposition rate of dissolved oxygen usually could not produce adequate intermediate radicals to achieve strong ECL intensity for biological detection.[7] In previous research studies, single-atom iron, TiO_2, and zirconium-based porphyrinic metal−organic framework nanoparticles (NMOFs) have been used as coreaction accelerators to boost the generation of reactive oxygen species (ROS) from dissolved oxygen.[7,9,10] Nevertheless, these coreaction accelerators needed a negative potential to reduce the dissolved oxygen, which might result in interferential reactions of other electroactive substances in the actual biosystem.[11−13] Herein, we employed Fe@Fe_2O_3

Received: July 22, 2021
Accepted: September 9, 2021
Published: September 23, 2021

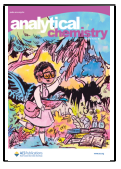

Downloaded via TSINGHUA UNIV on November 5, 2022 at 19:44:26 (UTC).
See https://pubs.acs.org/sharingguidelines for options on how to legitimately share published articles.

ACS Publications © 2021 American Chemical Society

https://doi.org/10.1021/acs.analchem.1c03102
Anal. Chem. 2021, 93, 13334−13341

Scheme 1. Schematic Diagram of (A) the Preparation of Fe@Fe_2O_3 Nanowires, (B) Possible Mechanism of the Proposed Ternary ECL System, (C) the Preparation of the T-Shaped Structure, (D) the Highly Efficient Strand Displacement Amplification, and (E) the Assembly Process of the ECL Biosensor

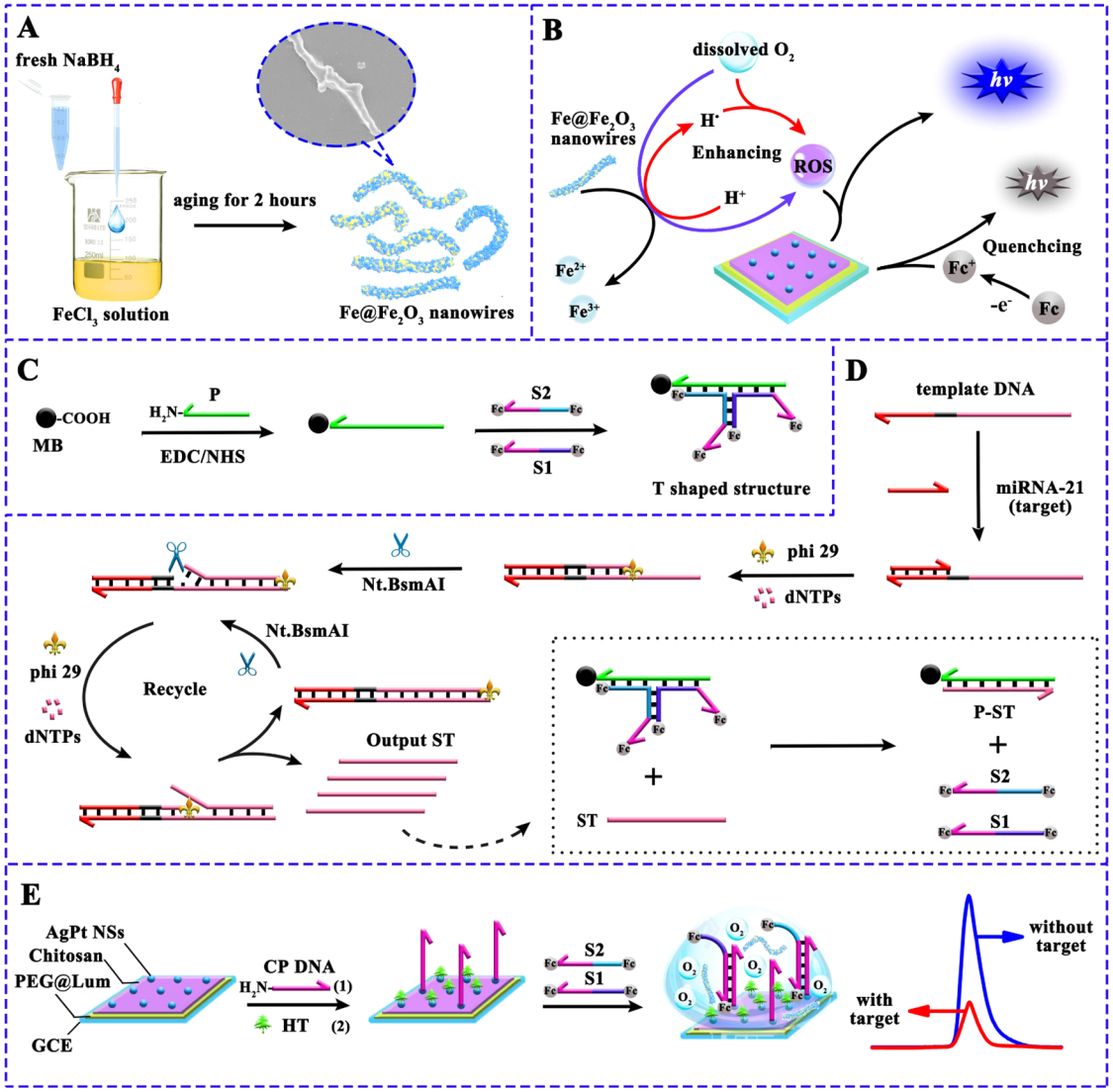

nanowires as a coreaction accelerator for the first time, which could produce ROS directly in the detection solution without the aid of a potential. As a result, this novel ternary ECL system (luminol/dissolved oxygen/ Fe@Fe_2O_3 nanowires) narrowed the detection potential range to 0−0.6 V so as to benefit its practical use in bioassays.

Strand displacement amplification (SDA) has been an efficient nucleic acid signal amplification strategy to produce numerous single-stranded DNA with the assistance of DNA polymerase and restriction endonucleases. However, for the traditional SDA reaction, only one strand is produced through each round of complete polymerization; hence, the amplification efficiency is limited and needs to be improved. Herein, an SDA coupled with strand displacement reaction (SDA-SDR) was first designed, in which two single-stranded DNAs were exported by disassembling a prepared T-shaped structure through SDR to enhance the signal amplification efficiency.

In this work, Fe@Fe_2O_3 nanowires were used as a novel coreaction accelerator of the luminol/dissolved oxygen system to construct an ultrasensitive biosensor for miRNA detection with the aid of a highly efficient strand displacement amplification (as shown in Scheme 1). In the presence of target miRNA-21, the SDA produced a great deal of secondary target (denoted as ST), which subsequently hybridized with the P strand in the prepared T-shaped structure (P-S1-S2) and dissociated S1 and S2 with Fc labeled at both 5′ and 3′ ends (Scheme 1D) to combine with the capture DNA (CP DNA) on the electrode for highly efficient quenching of the ECL signal (Scheme 1E). Therefore, an ultrasensitive biosensor was constructed for the analysis of miRNA-21 from cancer cell (MCF-7) lysate. The proposed biosensor provided a H_2O_2-free avenue for the luminol/dissolved oxygen ECL system and an ultrasensitive clinical diagnosis method of great promise.

EXPERIMENTAL SECTION

Synthesis of Fe@Fe_2O_3 Nanowires. Fe@Fe_2O_3 nanowires were prepared referring to the previous literature with minor changes.[14] Typically, 30 mg of $FeCl_3$ was dissolved in 10 mL of deionized water to form a clear yellow solution in a 50 mL beaker and then 4 mL of freshly prepared cold $NaBH_4$ solution (60 mg $NaBH_4$) was added dropwise into the above

https://doi.org/10.1021/acs.analchem.1c03102
Anal. Chem. 2021, 93, 13334−13341

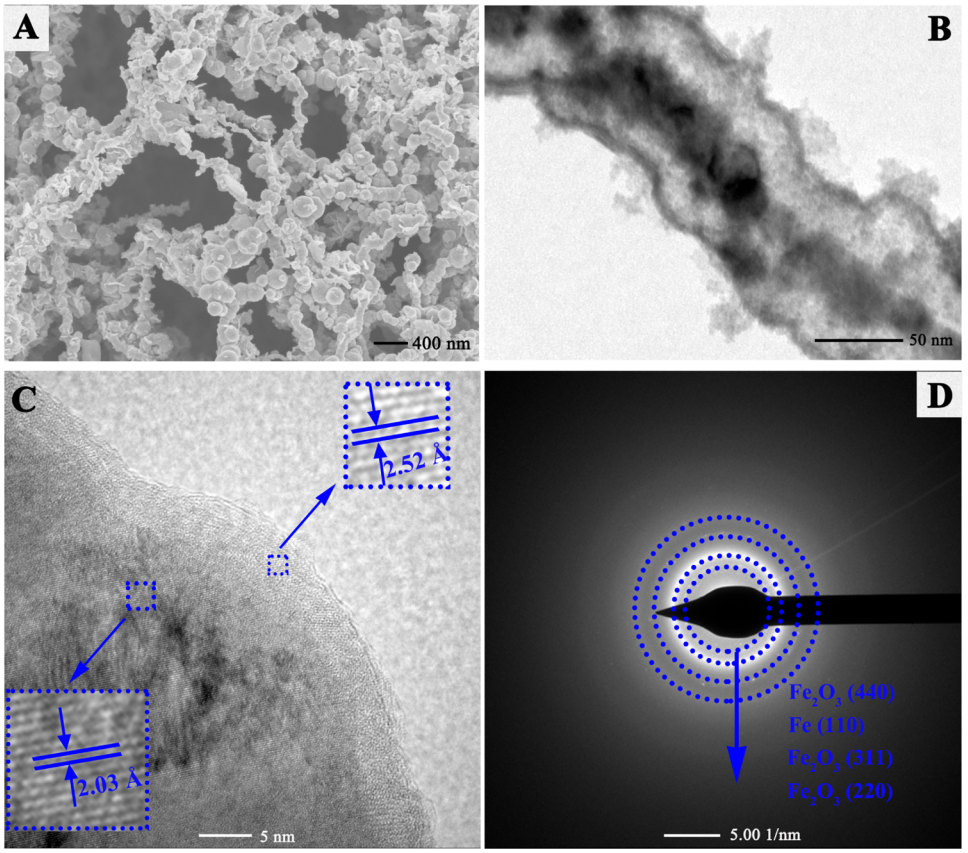

Figure 1. (A) SEM, (B) TEM, (C) HRTEM, and (D) SAED images of Fe@Fe_2O_3 nanowires.

solution. With the addition of the $NaBH_4$ solution dropwise, bubbles appeared and burst, and fluffy black sediment appeared and sank. Then, the beaker was put aside for 2 h. Afterward, the sediment was washed with water and ethanol alternately 3 times. In the end, it was dried within a vacuum freezing dryer.

Preparation of PEG@luminol (PEG@Lum). For the preparation of PEG@Lum, 3.0 g of PEG 4000 was dissolved in 10 mL of deionized water. After that, 3 mg of luminol was added into the above solution, with ultrasound to generate a homogeneous suspension liquid. Then, the liquid was heated at 50 °C until the volume of the concentrated solution was condensed to 3 mL. Afterward, the concentrated solution of PEG@Lum was stored in a centrifuge tube at 4 °C.

Operation of SDA-SDR. At first, 10 μL of mixture solutions containing target miRNA-21 (various concentrations, 1 nM, 100 pM, 10 pM, 1 pM, 100 fM, 10 fM, 1 fM), template (1 nM), and secondary target (ST, 1 nM) was prepared with Tri-HCl buffer, which was annealed at 95 °C for 10 min, and then cooled to 20 °C at a rate of 2 °C/min. Afterward, with the addition of 1 mM dNTPs, 200 U/mL phi29, and 200 U/mL Nt.*Bsm*AI, 100 μL of mixtures was heated to 37 °C and kept for 2 h for the continuous reaction of polymerization and nicking to produce a mass of ST. Then, the reactions were ended by devitalizing the phi29 and Nt.*Bsm*AI with 20 min of thermal treatment at 65 °C. Finally, the SDA product was stored under 4 °C in a refrigerator when not in use.

For the preparation of the T-shaped structure, 10 μL of carboxyl-labeled magnetic beads (5 mg/mL) was added to a 40 μL EDC solution (100 mM), and the mixture was allowed to react for 15 min to activate the carboxyl groups on the magnetic beads. Then, 10 μL of NHS solution (100 mM) and 40 μL of P with amino labeled (2.5 μM) were added to the above mixture. The whole mixture was stirred for 1 h for the amide reaction to form P-modified magnetic beads. Later, magnetic separation was utilized to remove the unreacted P and other substances. Next, the P-modified magnetic beads were added into a 100 μL mixture solution (1 μM S1 and 1 μM S2) and reacted at 95 °C for 5 min and quickly cooled to form a T-shaped structure of P-S1-S2. After that, the mixture system was separated again with a magnet to remove redundant chemicals and dispersed in 100 μL of the aforementioned SDA product. Thereafter, the strand displacement reaction (SDR) was carried out at room temperature for 2 h, during which the T-shaped structure of P-S1-S2 was disassembled by ST combined with P, and S1 and S2 were dissociated to participate in the construction of the biosensor. Then, the magnetic separation was applied again but the supernatant liquids were collected. Ultimately, the supernatant liquids were stored in a refrigerator at 4 °C before use.

Assembly of the ECL Biosensor. To assemble the ECL biosensor, a batch of glassy carbon electrodes (GCE) were polished with alumina (0.3 μm and 50 nm) slurry carefully and washed with water and ethanol under ultrasound. Then, 10 μL of the as-prepared PEG@Lum was dripped on a clean and dried surface of GCE. As the PEG@Lum naturally dried in air and formed a film, 10 μL of chitosan solution (1%) and AgPt nanospheres (AgPt NSs) were dropped on the PEG@Lum-coated GCE and left air-dried in succession. Afterward, 10 μL of CP DNA (2.5 μM) was dropped on the above-modified electrodes and incubated in a refrigerator at 4 °C overnight. Later on, the electrodes were rinsed with PBS to remove the

https://doi.org/10.1021/acs.analchem.1c03102
Anal. Chem. 2021, 93, 13334−13341

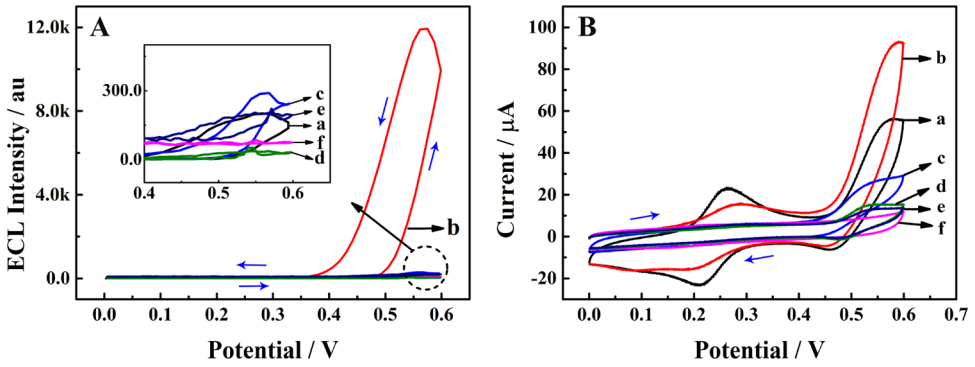

Figure 2. (A) ECL intensity−potential curves and (B) CV curves of GCE in (a) 0.6 mM luminol (air-saturated), (b) 0.6 mM luminol with 20 μg/mL $Fe@Fe_2O_3$ nanowires (air-saturated), (c) 0.6 mM luminol with 20 μg/mL $Fe@Fe_2O_3$ nanowires, and 1 mM L-cysteine (air-saturated), (d) 0.6 mM luminol (nitrogen-saturated), (e) 0.6 mM luminol with 20 μg/mL $Fe@Fe_2O_3$ nanowires (nitrogen-saturated), and (f) 20 μg/mL $Fe@Fe_2O_3$ nanowires (air-saturated).

uncombined CP DNA, and 10 μL of HT was incubated on the electrodes for 40 min to block the remaining specific sites of AgPt NSs.

Measurement Procedure. Overall, 10 μL of nucleic acid supernatant liquids mentioned above was dropped on the prepared biosensors and incubated at 37 °C for 80 min to allow S1 and S2 hybridization with the CP DNA. After that, the biosensors were rinsed with PBS to discard unbound reagents. Finally, in 2 mL of PBS with 25 μg/mL $Fe@Fe_2O_3$, ECL signals were tested within a three-electrode system on an MPI-E ECL analyzer using the cyclic voltammetry (CV) scan range of 0−0.6 V with the photomultiplier voltage set at 800 V.

RESULTS AND DISCUSSION

Characterization of the Prepared $Fe@Fe_2O_3$ Nanowires. Scanning electron microscopy (SEM), transmission electron microscopy (TEM), X-ray diffraction (XRD), X-ray photoelectron spectroscopy (XPS), and selected area electron diffraction (SAED) were employed to characterize the prepared $Fe@Fe_2O_3$ nanowires. Characterization of AgPt NSs is presented in the Supporting Information (Figure S2). As shown in Figure 1A, the $Fe@Fe_2O_3$ nanowires showed wirelike structures composed of nanoparticles. The diameter of nanowires ranged from 100 to 200 nm. In addition, energy-dispersive X-ray spectroscopy (EDS) images (Figure S1) demonstrated the presence of Fe and O elements. Furthermore, TEM images (Figure 1B) displayed the inner structure of the nanowires. In Figure 1B, a core−shell structure with clear dark and shade layers could be seen in the nanowires, which indicated that the interior Fe was wrapped by the exterior oxides. Besides, the XPS curves are presented in Figure S2. The full spectrum (Figure S2C) showed the coexistence of Fe, O, and C elements on the surface of the prepared sample. The carbon element was probably from adventitious exposure to carbon dioxide and hydrocarbon compounds in air and water during the preparation and transfer of the sample.[15] In the spectrum of Fe 2p (Figure S2A), two peaks at 707.0 and 719.9 eV corresponded to the binding energies of $2p_{3/2}$ and $2p_{1/2}$ of the metallic iron, respectively.[16] Meantime, two peaks at 713.1 and 725.8 eV were ascribed to the binding energies of $2p_{3/2}$ and $2p_{1/2}$ of Fe^{3+}, respectively,[17] while two peaks at 710.6 and 724.4 eV belonged to $2p_{3/2}$ and $2p_{1/2}$ of Fe^{2+}, respectively,[18] which was the ferrous iron adsorbed on the surface of nanowires from the solution.[19] In Figure S2B, a high-resolution spectrum of O 1s is displayed, which was fitted into two peaks at 530.0 and 531.4 eV. The peak at 530.0 eV was assigned to the Fe−O bond in Fe_2O_3, and the peak at 531.4 eV was attributed to −OH and H_2O adsorbed on the surface of the sample.[20] In addition, the XRD was utilized, and the patterns (Figure S2D) revealed distinct diffraction at 44.7°, which was attributed to the (110) crystal plane of metallic iron (PDF#06-0609), and a weak peak at 35.63° was from the (311) crystal plane of amorphous Fe_2O_3 (PDF#39-1346). In addition, the high-resolution TEM (HRTEM) images (Figure 1C) showed clear lattice fringes of 2.03 and 2.52 Å, which were the lattice spacings of Fe (110) and Fe_2O_3 (311) planes, respectively.[21] The SAED patterns (Figure 1D) showed that four concentric rings corresponded to Fe_2O_3 (440), Fe (110), Fe_2O_3 (311), and Fe_2O_3 (220) crystal planes.[22,23] Therefore, the above results suggested the successful preparation of $Fe@Fe_2O_3$ nanowires.

Exploration of the ECL Mechanism of the Ternary System. To study the mechanism of the proposed system, a series of controlled experiments were devised. As depicted in Figure 2A, the binary system (luminol/dissolved oxygen) only showed an ECL intensity of about 201 au (Figure 2A curve a). After $Fe@Fe_2O_3$ nanowires were added, the ECL intensity of the ternary system dramatically increased to 11937 au (Figure 2A curve b), about 58 times stronger than that of the binary system, which indicated that $Fe@Fe_2O_3$ nanowires could efficiently enhance the ECL performance of the luminol/dissolved oxygen system. Meanwhile, in Figure 2B, comparing curve b with curve a, the oxidation peak ascribed to the electrical oxidation of luminol at 0.55 V was evidently enhanced, and the reduction and oxidation peaks of oxygen at 0.21 and 0.26 V weakened apparently, suggesting that the electrochemical oxidation of luminol was promoted with $Fe@Fe_2O_3$ nanowires added in the detection solution, while the electrochemical reactions of the dissolved oxygen reduced. This might be because the dissolved oxygen reacted with $Fe@Fe_2O_3$ nanowires more easily, and the chemical reactions between the dissolved oxygen and $Fe@Fe_2O_3$ nanowires accelerated the electrochemical oxidation of luminol; thus, the ECL signal was distinctly enhanced. Nevertheless, when L-cysteine was added to scavenge ROS in the detection solution, the ECL response plummeted to 22 au (Figure 2A curve c), and the redox peaks of the dissolved oxygen in CV waves disappeared (Figure 2B curve c), suggesting that $Fe@Fe_2O_3$ nanowires boosted the ECL intensity of the luminol/dissolved oxygen system by promoting the production of numerous

https://doi.org/10.1021/acs.analchem.1c03102
Anal. Chem. 2021, 93, 13334−13341

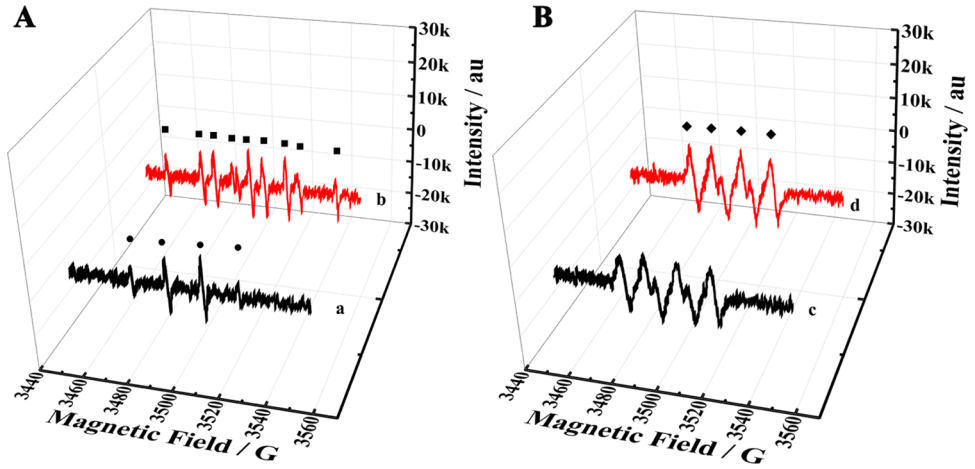

Figure 3. (A) EPR spectra for DMPO-$OH^{\bullet}$ of $Fe@Fe_2O_3$ nanowires in (a) water and (b) PBS. (B) EPR spectra for DMPO-$O_2^{\bullet-}$ of $Fe@Fe_2O_3$ nanowires in (c) 50% methanol aqueous solution and (d) 50% methanol phosphate solution.

ROS. Similarly, when the dissolved oxygen in the detection system was dispelled by N_2, whether the $Fe@Fe_2O_3$ nanowires were present or not, the ECL emissions were both fairly weak (Figure 2A curves d and e), and the redox peaks of the dissolved oxygen in CV waves vanished (Figure 2B curves d and e), which demonstrated that $Fe@Fe_2O_3$ nanowires could not work without the participation of dissolved oxygen. In addition, when there was no luminol in the system, no ECL peak emerged in the ECL intensity−potential curve (Figure 2A curve f), and also the oxidation peak at 0.55 V disappeared (Figure 2B curve f), implying that in the ternary system the luminophore was luminol rather than dissolved oxygen or $Fe@Fe_2O_3$ nanowires. Thus, the $Fe@Fe_2O_3$ nanowires could be defined as an ECL coreaction accelerator for the luminol/dissolved oxygen system, which did not interact with luminol directly but by accelerating the generation of plentiful ROS to improve the ECL emission of the system.

Possible Enhancement Mechanism of the $Fe@Fe_2O_3$ Nanowires for the Luminol/Dissolved Oxygen System. To investigate the specific working principles of $Fe@Fe_2O_3$ nanowires in the ternary system, electron paramagnetic resonance (EPR) experiments were carried out to trap the involved reactive radicals in the ECL process with 5,5-dimethyl-1-pyrroline-*N*-oxide (DMPO) as a spin-trapping agent. Since a previous study has reported the impact of phosphate on the generation of ROS from the oxygen reduction reaction predominated by $Fe@Fe_2O_3$,[1414] herein four experimental conditions were built to trace the possible ROS related to the ternary ECL system. First, as shown in Figure 3A, in an aqueous solution of $Fe@Fe_2O_3$ nanowires (Figure 3A curve a), typical quartet peaks (relative intensity 1:2:2:1) with a hyperfine splitting constant of $\alpha_N = \alpha_H = 14.9$ G were observed, which were the evident spectrum of the DMPO-$OH^{\bullet}$ adduct.[24,25] However, in the PBS solution of $Fe@Fe_2O_3$ nanowires (Figure 3A curve b), a diagram of new signals appeared ($\alpha_N = 16.5$ G, $\alpha_H = 22.5$ G), confirming the generation of $H^{\bullet}$,[26] while the signal of $OH^{\bullet}$ became unapparent because of the strong signal of $H^{\bullet}$ and the superposition of the DMPO-$OH^{\bullet}$ signal with the DMPO-$H^{\bullet}$ signal. To check the generation of $O_2^{\bullet-}$, the 50% methanol aqueous solution of $Fe@Fe_2O_3$ nanowires was examined (Figure 3B curve c), and the characteristic spectrum of the DMPO-$O_2^{\bullet-}$ adduct ($\alpha_N = 12.9$ G, $\alpha_H = 10.2$ G and 1.5 G) confirmed the generation of $O_2^{\bullet-}$.[27] In contrast, when the water in the methanol solution was replaced by the PBS solution, no remarkable change occurred in the DMPO-$O_2^{\bullet-}$ signal (Figure 3B curve d). Therefore, it could be inferred that three kinds of intermediate radicals were involved in the ECL process of the luminol/dissolved oxygen/$Fe@Fe_2O_3$ nanowires system. As dissolved oxygen can quickly react with $H^{\bullet}$ to produce $OOH^{\bullet}$, the ECL mechanism in the ternary system could be portrayed as follows (LH^- represented luminol anion, $L^{\bullet-}$ represented luminol anionic radicals, and AP^{2-*} represented excited-state species 3-aminophthalate).

$$LH^- - e^- \rightarrow LH^{\bullet} \rightarrow L^{\bullet-} + H^+ \quad (1)$$

$$Fe + 2H^+ \rightarrow 2H^{\bullet} + Fe^{2+} \quad (2)$$

$$H^{\bullet} + O_2 \rightarrow OOH^{\bullet} \leftrightarrow O_2^{\bullet-} + H^+ \quad (3)$$

$$O_2 + Fe + 2H^+ \rightarrow Fe^{2+} + H_2O_2 \quad (4)$$

$$O_2 + Fe^{2+} \rightarrow O_2^{\bullet-} + Fe^{3+} \quad (5)$$

$$H_2O_2 + Fe^{2+} \rightarrow OH^{\bullet} + OH^- + Fe^{3+} \quad (6)$$

$$L^{\bullet-} + O_2^{\bullet-} \rightarrow LO_2^{2-} \rightarrow AP^{2-*} + N_2 \quad (7)$$

$$AP^{2-*} \rightarrow AP^{2-} + h\nu \quad (8)$$

$$Fc - e^- \rightarrow Fc^+ \quad (9)$$

$$Fc^+ + O_2^{\bullet-} \rightarrow Fc + O_2 \quad (10)$$

$$Fc^+ + AP^{2-*} \rightarrow \text{product} + Fc \quad (11)$$

First, luminol was deprotonated to LH^-, which was further electrochemically oxidized to $L^{\bullet-}$ (eq 1). Then, the reduction process of the dissolved oxygen to ROS could be divided into two routes. In route I, Fe core in the $Fe@Fe_2O_3$ nanowires reacted with H^+ to produce $H^{\bullet}$ (eq 2), and the dissolved oxygen quickly trapped $H^{\bullet}$ to form $OOH^{\bullet}$, which could mutually transform to $O_2^{\bullet-}$ (eq 3).[14] In route II, the dissolved oxygen was reduced to H_2O_2 by the Fe core (eq 4) or to $O_2^{\bullet-}$ by Fe^{2+} on the surface of the Fe_2O_3 oxidation layer (eq 5).[14] H_2O_2 was decomposed to $OH^{\bullet}$ and OH^- by Fe^{2+} (eq 6).[28] In turn, the formation of OH^- could promote the deprotonation process and the reaction of eq 1 to produce more $L^{\bullet-}$. Finally,

https://doi.org/10.1021/acs.analchem.1c03102
Anal. Chem. 2021, 93, 13334−13341

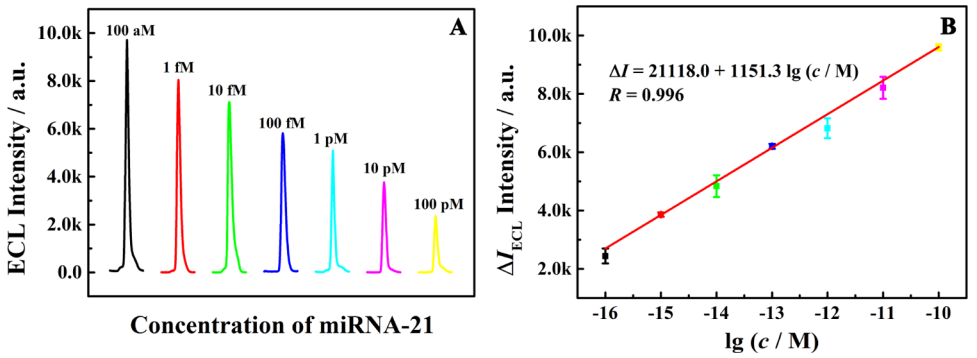

Figure 4. (A) ECL intensity of the fabricated biosensor with different concentrations of miRNA-21 from 100 aM to 100 pM and (B) calibration curve and equation of the miRNA-21 detection (S/N = 3).

Table 1. Comparison of Other Methods and this Work for miRNA Detection

analytical method	target	linearity range	LOD	reference
fluorescence	miRNA-21	1 pM ~ 10 nM	0.35 pM	29
fluorescence	miRNA-21	10 fM ~ 1 pM	1 fM	30
electrochemical	miRNA-21	0.5 fM ~ 100 nM	0.25 fM	31
SERS	miRNA-21	1 fM ~ 10 nM	0.34 fM	32
ECL	miRNA-155	0.5 fM ~ 100 pM	0.1 fM	33
ECL	miRNA-133a	500 fM ~ 1 nM	60 fM	34
ECL	miRNA-21	100 aM ~ 100 pM	52.5 aM	present work

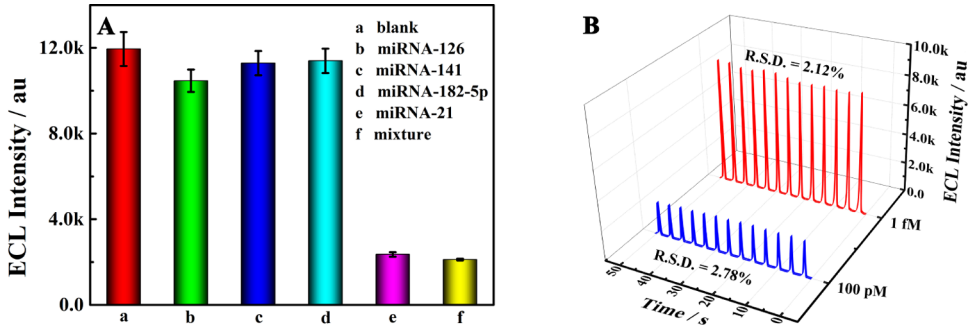

Figure 5. (A) Selectivity of the proposed biosensor against three interference miRNAs, and (B) stability of the biosensor with 1 fM and 100 pM miRNA-21 under 13 cycles of potential scans.

$L^{\bullet-}$ reacted with $O_2^{\bullet-}$ and produced an unstable excited-state species AP^{2-}* (eq 7), which underwent a radiative reaction and released luminescence (eq 8). Specifically, after the introduction of ferrocene (Fc) in the luminol/dissolved oxygen system, the ECL-quenching mechanism could be explained as follows. Under anodic potential scan, Fc was oxidized to ferrocenium (Fc^+, eq 9). Afterward, Fc^+ quenched the ECL by capturing an electron from $O_2^{\bullet-}$ (eq 10) or annihilating the excited-state species AP^{2-}* (eq 11).

Detection of miRNA-21 with the Proposed Biosensor. The feasibility of the proposed nucleic acid signal amplification strategy and the characterization of the biosensor assembly process are demonstrated in the Supporting Information. Before detection of miRNA, two critical experimental conditions, the reaction time of SDA and the hybridization time between CP DNA and S1 and S2 were explored to maximize the performance of the proposed biosensor (the results are shown in Figure S4). Under optimum conditions, the progressive increase of the concentration of miRNA-21 contributed to a continuously decreased ECL signal (Figure 4A). As displayed in Figure 4B, in the range of 100 aM−100 pM, ΔI (the decreasing amount of ECL intensity in target detection compared to blank test, $\Delta I = I_B - I$; the blank test was performed by replacing the target with Tri-HCl buffer) was linearly related to the logarithm of the target concentration. The linear relationship could be described as ΔI = 21118.0 + 1151.3 lg(c/M), and the limit of detection (LOD) was calculated to be 52.5 aM (the detailed calculation process is described in the Supporting Information). In addition, the comparison between this designed biosensor and some other reported strategies is exhibited in Table 1, suggesting that the proposed method had superior sensitivity.

Selectivity and Stability of the Designed Biosensor. To test the selectivity of the biosensor, three interference miRNAs (miRNA-126, miRNA-141, and miRNA-182-5p) were employed to substitute miRNA-21 and conducted the same detection procedure. As depicted in Figure 5A, when miRNA-126, miRNA-141, and miRNA-182-5p (10 nM) were used, the ECL signals were almost equal to the blank test, demonstrating that the fabricated biosensor had no obvious response to these nonspecific miRNAs. Moreover, when miRNA-21 (100 pM) was mixed with these interfering miRNAs (10 nM), the ECL signal had no distinct change in contrast to that when only miRNA-21 (100 pM) was involved,

https://doi.org/10.1021/acs.analchem.1c03102
Anal. Chem. 2021, 93, 13334−13341

suggesting that these miRNAs did not cause an apparent effect to the detection of miRNA-21. Hence, the proposed biosensor possessed excellent specificity and selectivity to miRNA-21.

Stability is another important property of biosensors. As demonstrated in Figure 5B, with 1 fM and 100 pM miRNA-21 used on the biosensor, under 13 cycles of continuous CV scans, there were merely perceptible changes to the ECL intensity with relative standard deviations (R.S.D.) of 2.12 and 2.78% respectively, verifying that the constructed biosensor had excellent stability.

Application of the Constructed Biosensor in Cancer Cell Assays. To evaluate the practical application performance of the designed biosensor, two kinds of cell lysates (human breast cancer cell MCF-7 and cervical cancer cell Hela) were used to play the role of miRNA-21 standard solutions. The lysates were obtained by an RNA extraction kit after cell counting. In Figure 6, with the number of cells increasing from

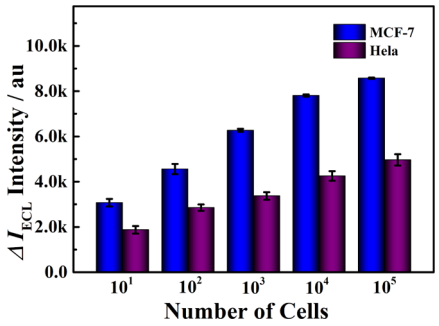

Figure 6. Application of the constructed biosensor for the detection of miRNA-21 from MCF-7 and Hela cell lysates.

10 to 10^5, ΔI aggrandized orderly in both MCF-7 and Hela cell analyses. Obviously, the increment of MCF-7 lysate assays was more notable than Hela, which was consistent with the fact that the expression level of miRNA-21 in MCF-7 is higher than in Hela.[35] Consequently, these results certified that the proposed biosensor exhibited favorable practicability in actual sample detection.

CONCLUSIONS

In short, this work combined a novel H_2O_2-free ternary (ECL) system with highly efficient strand displacement amplification (SDA) for sensitive detection of miRNA-21 in human cancer cells. Specifically, Fe@Fe_2O_3 nanowires were used as an effective coreaction accelerator to translate dissolved oxygen to a large collection of reactive oxygen species (ROS) for a distinct promotion of ECL signal, which did not need the excitation of voltage and thus narrowed the potential range for the avoidance of side reactions and improvement of its possibility in practical bioanalysis. In addition, an original SDA-SDR strategy was proposed to improve signal amplification efficiency for ultrasensitive detection of miRNA-21. Satisfactorily, the constructed biosensor could be successfully utilized to analyze miRNA-21 from human cancer cell (MCF-7) lysates. Besides, this work not only just provided a H_2O_2-free method for a versatile luminol/dissolved oxygen system but also created a promising analysis method for clinical biomarker assays.

ASSOCIATED CONTENT

Supporting Information

The Supporting Information is available free of charge at https://pubs.acs.org/doi/10.1021/acs.analchem.1c03102.

Experimental operation and related experimental characterization (PDF)

AUTHOR INFORMATION

Corresponding Authors

Ya-Qin Chai − *Key Laboratory of Luminescence Analysis and Molecular Sensing (Southwest University), Ministry of Education, College of Chemistry and Chemical Engineering, Southwest University, Chongqing 400715, P. R. China;* orcid.org/0000-0003-4392-9592; Phone: +86-23-68252277; Email: yqchai@swu.edu.cn; Fax: +86-23-68253172

Ruo Yuan − *Key Laboratory of Luminescence Analysis and Molecular Sensing (Southwest University), Ministry of Education, College of Chemistry and Chemical Engineering, Southwest University, Chongqing 400715, P. R. China;* orcid.org/0000-0003-3664-6236; Email: yuanruo@swu.edu.cn

Authors

Jia-Li Liu − *Key Laboratory of Luminescence Analysis and Molecular Sensing (Southwest University), Ministry of Education, College of Chemistry and Chemical Engineering, Southwest University, Chongqing 400715, P. R. China*

Rong Yang − *Key Laboratory of Luminescence Analysis and Molecular Sensing (Southwest University), Ministry of Education, College of Chemistry and Chemical Engineering, Southwest University, Chongqing 400715, P. R. China*

Complete contact information is available at: https://pubs.acs.org/10.1021/acs.analchem.1c03102

Author Contributions

†J.-L.L. and R.Y. are co-first authors.

Notes

The authors declare no competing financial interest.

ACKNOWLEDGMENTS

This work was financially supported by the National Natural Science Foundation of China (21974108, 21775124, and 21675129).

REFERENCES

(1) Yokoi, A.; Matsuzaki, J.; Yamamoto, Y.; Yoneoka, Y.; Takahashi, K.; Shimizu, H.; Uehara, T.; Ishikawa, M.; Ikeda, S.; Sonoda, T.; Kawauchi, J.; Takizawa, S.; Aoki, Y.; Niida, S.; Sakamoto, H.; Kato, K.; Kato, T.; Ochiya, T. *Nat. Commun.* **2018**, *9*, No. 4319.

(2) Xue, T. Y.; Liang, W. Y.; Li, Y. W.; Sun, Y. H.; Xiang, Y. J.; Zhang, Y. P.; Dai, Z. G.; Duo, Y. H.; Wu, L. M.; Qi, K.; Shivananju, B. N.; Zhang, L. J.; Cui, X. Q.; Zhang, H.; Bao, Q. L. *Nat. Commun.* **2019**, *10*, No. 28.

(3) Ma, W.; Fu, P.; Sun, M. Z.; Xu, L. G.; Kuang, H.; Xu, C. L. *J. Am. Chem. Soc.* **2017**, *139*, 11752−11759.

(4) Xu, Z. H.; Wang, H.; Wang, J.; Zhao, W.; Xu, J. J.; Chen, H. Y. *Anal. Chem.* **2019**, *91*, 12000−12005.

(5) Du, Y.; Xue, J. W.; Sun, X.; Wu, D.; Liu, X. J.; Ju, H. X.; Yang, L.; Wei, Q. *Anal. Chem.* **2020**, *92*, 8472−8479.

(6) Zhang, Y. M.; Wang, F.; Zhang, H. X.; Wang, H. Y.; Liu, Y. *Anal. Chem.* **2019**, *91*, 12100−12107.

(7) Gu, W. L.; Wang, H. J.; Jiao, L.; Wu, Y.; Chen, Y. X.; Hu, L. Y.; Gong, J. M.; Du, D.; Zhu, C. Z. *Angew. Chem., Int. Ed.* **2020**, *59*, 3534−3538.
(8) Gu, W. L.; Wang, X. S.; Wen, J.; Cao, S. Y.; Jiao, L.; Wu, Y.; Wei, X. Q.; Zheng, L. R.; Hu, L. Y.; Zhang, L. Z.; Zhu, C. Z. *Anal. Chem.* **2021**, *93*, 8663−8670.
(9) Liang, J. L.; Xu, Q. H.; Teng, X.; Guan, W. J.; Lu, C. *Anal. Chem.* **2020**, *92*, 1628−1634.
(10) Zhang, G. Y.; Chai, H. N.; Tian, M. W.; Zhu, S. F.; Qu, L. J.; Zhang, X. J. *Anal. Chem.* **2020**, *92*, 7354−7362.
(11) Fu, L.; Zhang, B.; Fu, K. N.; Gao, X. W.; Zou, G. Z. *Anal. Chem.* **2020**, *92*, 6144−6149.
(12) Wang, C.; Han, Q.; Mo, F. J.; Chen, M.; Xiong, Z. W.; Fu, Y. Z. *Anal. Chem.* **2020**, *92*, 12145−12151.
(13) Song, Y.; Zhang, W.; He, S. J.; Shang, L.; Ma, R. N.; Jia, L. P.; Wang, H. S. *ACS Appl. Mater. Interfaces* **2019**, *11*, 33676−33683.
(14) Mu, Y.; Ai, Z. H.; Zhang, L. Z. *Environ. Sci. Technol.* **2017**, *51*, 8101−8109.
(15) Shen, W. J.; Mu, Y.; Wang, B. N.; Ai, Z. H.; Zhang, L. Z. *Appl. Surf. Sci.* **2017**, *393*, 316−324.
(16) Tang, X. N.; Cao, R.; Li, L. B.; Huang, B. Y.; Zhai, W. J.; Yuan, K.; Chen, Y. W. *J. Mater. Chem. A* **2020**, *8*, 25919−25930.
(17) Ma, M. R.; Zhu, H.; Ling, J.; Gong, S. Q.; Zhang, Y.; Xia, Y. S.; Tang, Z. Y. *ACS Nano* **2020**, *14*, 4036−4044.
(18) Li, J.; Xiao, C.; Wang, K.; Li, Y.; Zhang, G. K. *Environ. Sci. Technol.* **2019**, *53*, 11023−11030.
(19) Ai, Z. H.; Gao, Z. T.; Zhang, L. Z.; He, W. W.; Yin, J. J. *Environ. Sci. Technol.* **2013**, *47*, 5344−5352.
(20) Khatun, S.; Roy, P. *Chem. Commun.* **2020**, *56*, 7293−7296.
(21) Xiao, Z. R.; Wu, C.; Wang, W.; Pan, L.; Zou, J. J.; Wang, L.; Zhang, X. W.; Li, G. Z. *J. Mater. Chem. A* **2020**, *8*, 25791−25804.
(22) Aslam, M.; Qamar, M. T.; Rehman, A. U.; Soomro, M. T.; Ali, S.; Ismail, I.; Hameed, A. *Appl. Surf. Sci.* **2018**, *451*, 128−140.
(23) He, L.; Wu, H. Y.; Zhang, W. Y.; Bai, X.; Chen, J. K.; Ikram, M.; Wang, R. H.; Shi, K. Y. *J. Hazard. Mater.* **2021**, *405*, No. 124252.
(24) Wang, Z. J.; Sun, P. Z.; Li, Y. X.; Meng, T.; Li, Z. P.; Zhang, X.; Zhang, R. C.; Jia, H. Z.; Yao, H. *Environ. Sci. Technol.* **2019**, *53*, 12688−12696.
(25) Zhang, R. C.; Li, Y. X.; Wang, Z. J.; Tong, Y. D.; Sun, P. Z. *Water Res.* **2020**, *177*, No. 115809.
(26) Miyaji, A.; Kohno, M.; Inoue, Y.; Baba, T. *Biochem. Biophys. Res. Commun.* **2017**, *483*, 178−182.
(27) Cui, J. X.; Wang, X.; Zheng, K. Y.; Wang, D. H.; Zhu, H.; Mao, X. H. *Environ. Sci. Technol.* **2020**, *54*, 1242−1249.
(28) Liu, Y.; Zhao, Y.; Wang, J. L. *J. Hazard. Mater.* **2021**, *404*, No. 124191.
(29) Yang, Z. Z.; Peng, X.; Yang, P.; Zhuo, Y.; Chai, Y. Q.; Liang, W. B.; Yuan, R. *Chem. Sci.* **2020**, *11*, 8482−8488.
(30) Li, B. X.; Liu, Y. J.; Liu, Y. X.; Tian, T. T.; Yang, B. B.; Huang, X. D.; Liu, J. W.; Liu, B. H. *ACS Nano* **2020**, *14*, 8116−8125.
(31) Zhang, X. L.; Yang, Z. H.; Chang, Y. Y.; Liu, D.; Li, Y. R.; Chai, Y. Q.; Zhuo, Y.; Yuan, R. *Chem. Sci.* **2020**, *11*, 148−153.
(32) Wen, S. P.; Su, Y.; Dai, C. X.; Jia, J. R.; Fan, G. C.; Jiang, L. P.; Song, R. B.; Zhu, J. J. *Anal. Chem.* **2019**, *91*, 12298−12306.
(33) Lu, L. P.; Wang, J. X.; Miao, W. J.; Wang, X. Y.; Guo, G. S. *Anal. Chem.* **2019**, *91*, 1452−1459.
(34) Ye, J.; Liu, G. Y.; Yan, M. X.; Zhu, Q. J.; Zhu, L. P.; Huang, J. S.; Yang, X. R. *Anal. Chem.* **2019**, *91*, 13237−13243.
(35) Liu, L. L.; Zhang, Y.; Yuan, R.; Wang, H. J. *Anal. Chem.* **2020**, *92*, 15112−15119.

https://doi.org/10.1021/acs.analchem.1c03102
Anal. Chem. 2021, 93, 13334−13341